Original article

Institution of MECHANICAL ENGINEERS

Journal of MATERIALS: DESIGN AND APPLICATIONS

Proc IMechE Part L:
J Materials: Design and Applications
0(0) 1–17

DOI: 10.1177/1464420717708486
journals.sagepub.com/home/pil

SAGE

Numerical implementation of the microplane constitutive model for shape memory alloys

MR Karamooz-Ravari[1] and B Shahriari[2]

Abstract

With the advent of shape memory alloys, several industrial applications were proposed due to their superior mechanical and biological properties. Since the fabrication and characterization of shape memory alloy devices is challenging and expensive, it is necessary to simulate their thermomechanical responses before fabrication. To do so, a powerful constitutive model capable of simulation of the important features of these materials is necessary. To be able to simulate a shape memory alloy device, it is vital to implement a suitable constitutive model in such a way to be used in finite element models. In this paper, an existing constitutive model based on microplane theory is numerically implemented and the effects of stress increment, different numerical integration formulas, and loading direction on the thermomechanical response of shape memory alloy is investigated through superelastic and shape memory proportional and nonproportional loadings. The obtained results show that the stress increment may have significant effect on the results if the forward Euler scheme is utilized. In addition, for the case of numerical integration over the surface of a unit hemisphere, 61 points integration formula without orthogonal symmetry provides the best results while 21 orthogonally symmetric one is the most inaccurate one. Also, the orthogonally symmetric numerical integration formulas predict the isotropic material response while those without orthogonal symmetry predict a little anisotropy.

Keywords

Microplane theory, constitutive modeling, numerical integration, shape memory alloys, shape memory effect, superelasticity

Date received: 22 February 2017; accepted: 16 April 2017

Introduction

After the discovery of shape memory alloys (SMA) in 1962 by Buehler et al.,[1] the researchers have been attracted to utilizing these alloys in different industries such as aerospace, biomedical, civil, automobile, and robotics because of their superior mechanical and biological properties. Although the use of such materials may increase the performance of new advanced devices, the final cost of those devices would also be increased due the price of raw material as well as the fabrication procedure.[2] In order to reduce the costs of such fabrications, it is necessary to assess the responses of a desired device using numerical models before fabrication. To do so, a powerful constitutive model is needed to be able to simulate the constitutive behavior of the material.

Since the 80th decade, several 1D and 3D constitutive models have been proposed for the SMAs. The main aim of these constitutive models is to simulate the complicated thermomechanical behavior of these alloys including superelasticity, shape memory effect, asymmetric material response,[3–11] different material properties of austenite and martensite,[12] cyclic loading,[13] and thermomechanical coupling.[14–16] These constitutive models can be categorized into two major groups,[17] i.e. microscopic thermodynamics models[18–22] and macroscopic phenomenological models.[6,15,16,23–30]

The microscopic models, such as those based on crystal plasticity,[31–33] focus mainly on the microscopic details of the material, so they are suitable for the investigation of the microstructural features such as the deformation mechanisms. Since these models are not computationally efficient, they are rarely used in the engineering applications. The phenomenological

[1]Department of Mechanical Engineering, Graduate University of Advanced Technology, Kerman, Iran
[2]Department of Mechanical and Aerospace Engineering, Malek-Ashtar University of Technology, Isfahan, Iran

Corresponding author:
MR Karamooz-Ravari, Department of Mechanical Engineering, Graduate University of Advanced Technology, Kerman 76311-33131, Iran.
Email: m.karamooz@kgut.ac.ir

models are developed based on the phenomenological thermodynamics or by direct use of the experimental responses. Due to their simplicity and low computational costs, these models are suitable for the engineering applications. However, they can only provide the macroscopic response of SMAs and do not include the microscopic features. Since these models are often based on a phase diagram, which is obtained using the experimental data, they have sufficient accuracy. Some of the most well-known phenomenological models are polynomial potential, hysteresis, phase transformation kinetics, and microplane model.[34]

Whichever method is used for modeling of the constitutive response of SMAs, it is inevitable to numerically implement it using an incremental process that can be used in combination with the finite element method. Qidwai and Lagoudas[35] presented a comprehensive study on the numerical implementation of SMA thermomechanical constitutive response using return mapping algorithms i.e. elastic predictor-transformation corrector. Arghavani et al.[36] developed constitutive models at small and finite strain regimes and then investigated solution algorithm, robustness, and computational cost or efficiency for the latter.[37] Wang et al.[38] presented a constitutive model for SMAs considering permanent deformations and then implemented it as user material subroutine (UMAT) into ABAQUS/Standard. Hartl and Lagoudas[39] proposed a constitutive model for SMAs to take the initiation and evolution of plastic strains into account. They then implemented it numerically in a finite element framework using a return mapping algorithm to solve the constitutive equations at each material point. Arghavani et al.[24] developed a finite strain kinematic hardening constitutive model for SMAs based on Hencky strain. Introducing a logarithmic mapping, they also presented an appropriate form of the proposed constitutive equations in the time-discrete frame. Stebner and Brinson[40] implemented an improved three-dimensional constitutive model for SMAs through explicit finite element method. They assessed the simulation time and convergence of the numerical process for single as well as multi element models. Auricchio et al.[41] used Fischer–Burmeister complementarity function instead of the classical set of Kuhn–Tucker inequality conditions to enhance the effectiveness and efficiency of numerical procedure for implementation of SMA constitutive model.

Referring to the literature, there are lots of constitutive models for the simulation of thermomechanical response of SMAs, among which, microplane theory is vastly used for this purpose because it just uses the material parameters obtained in simple tension (compression) test for the simulation of the 3D response of the material.[11] The basis of the method was established by Taylor in 1938 known as "slip theory of plasticity". However, the word "microplane" was first used by Bazant in 1984 and used for the simulation of the mechanical response of concrete.[42] This method was utilized by Brocca et al.[43] for the constitutive modeling of SMAs for the first time. It was then modified by Kadkhodaei et al.,[44,45] Mehrabi et al.,[45,46] and Karamooz Ravari et al.[11] and used for the simulation of the mechanical response of SMA devices.[47–50] However, there is a lack of a comprehensive numerical implementation of this constitutive model in the literature. To compensate this deficiency, in this paper the numerical implementation of the previously reported SMA constitutive model based on microplane theory is presented. To do so, first the tensorial formulation of this model is briefly reviewed and the Voigt notation of this formulation is presented. Then, the numerical implementation process is brought and different numerical integration schemes are introduced. Finally, the numerical results are obtained and the effects of stress increment size, numerical integration formula, and loading mode on the thermomechanical response of SMAs in shape memory and superelastic regimes are investigated.

Microplane constitutive model for SMAs

The key idea of microplane theory is to generalize 1D constitutive models to 3D ones, so one just needs the material parameters obtained using uniaxial tension (compression) to investigate the constitutive response of the material. To do so, three main steps must be followed. First, the stress tensor is projected on the generic planes passes through each material point known as microplane. Then, a suitable constitutive relation between the 1D micro-level stresses and strains are supposed. Finally, these 1D relations are generalized to a 3D constitutive model utilizing a homogenization process which, in this case, is the complementary virtual work. In this section, first, the tensorial derivation of the SMA constitutive model based on microplane theory is presented. Then, the Voigt notation of these formulation is derived for the numerical implementation purposes.

Tensorial derivation

As mentioned above, the first step toward the constitutive modeling based on microplane theory is to project the stress tensor on the microplanes. As shown in Figure 1, considering a microplane with

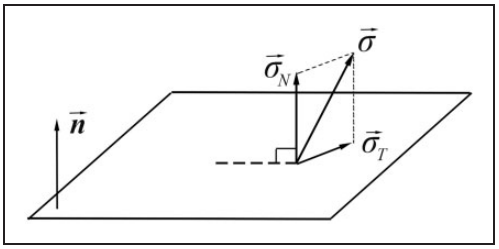

Figure 1. Projection of the stress vector on a microplane.

the normal unit vector, $\boldsymbol{n}$, the normal, σ_N, and tangential, σ_T, stress components can be formulated as follows[11]

$$\sigma_N = \sigma_{ij} n_i n_j \tag{1}$$

$$\sigma_T = \frac{1}{2}\sigma_{ij}\left(t_i n_j + t_j n_i\right) \tag{2}$$

where σ_{ij} is the stress tensor and t_i is the unit vector parallel to the tangential stress which can be formulated as

$$t_i = \frac{\sigma_{ij} n_j - \sigma_N n_i}{\sqrt{\sigma_{pq}\sigma_{pr} n_q n_r - \sigma_N^2}} \tag{3}$$

It has been previously shown[43,44] that by decomposing the normal component of stress vector into volumetric and deviatoric parts, i.e. $\sigma_N = \sigma_V + \sigma_D$, the micro-level elastic modulus is equal to the macroscopic one. In this relation, $\sigma_V = \frac{1}{3}\sigma_{ij}\delta_{ij}$ is the volumetric part, $\sigma_D = \left(n_i n_j - \frac{1}{3}\delta_{ij}\right)\sigma_{ij}$ the deviatoric part, and δ_{ij} the Kronecker's delta. In microplane theory it is supposed that the martensite transformation is only associated with the tangential stress. Accordingly, the following equations stand between 1D stresses and strains[50]

$$\epsilon_V = \frac{1-2\nu}{E}\sigma_V \tag{4}$$

$$\epsilon_D = \frac{1+\nu}{E}\sigma_D \tag{5}$$

$$\epsilon_T = \frac{1+\nu}{E}\sigma_T + \epsilon^* \xi_s \tag{6}$$

In the above relations, ν is the Poisson ration, E the elastic modulus, ϵ^* the maximum recoverable strain, and ξ_s the stress-induced martensite volume fraction. Since the elastic modulus of martensite and austenite phases are different, the elastic modulus of an SMA is changed during transformation. To account for this changes, the elastic modulus, E, is expressed using the Reuss model[11,44,45,48–50]

$$\frac{1}{E} = \frac{1-(\xi_T+\xi_s)}{E_A} + \frac{\xi_T+\xi_s}{E_M} \tag{7}$$

where E_A is the elastic modulus of pure austenite, E_M the elastic modulus of pure martensite, and ξ_T the temperature-induced martensite volume fraction. In order to fully quantify the strain components, it is necessary to define the stress- as well as temperature-induced martensite volume fractions as a function of stress and temperature. Referring to the phase diagram shown in Figure 2, at a given point, i, on an arbitrary loading path, , in the region, R_k, the stress- and temperature-induced martensite volume fractions can be calculated using the following phenomenological evolution[51]

$$\xi_{i,q} = \begin{cases} f_{i,q}\left(\xi_{i,s0}, \xi_{i,T0}, \tau_i, \overline{\sigma_i}, T_i\right) & \text{if } i \in R_k \text{ and } \tau_i \cdot n_k > 0 \\ \xi_{i0,q} & \text{otherwise} \end{cases} \tag{8}$$

where T is the temperature, τ the tangent vector of the loading path, $\bar{\sigma}$ the equivalent von Mises stress, and ξ_{s0} and ξ_{T0} are the initial values of stress- and temperature-induced martensite volume fractions, respectively. The subscript, i, denote the given point, and the subscript q stands for s and T. The evolution

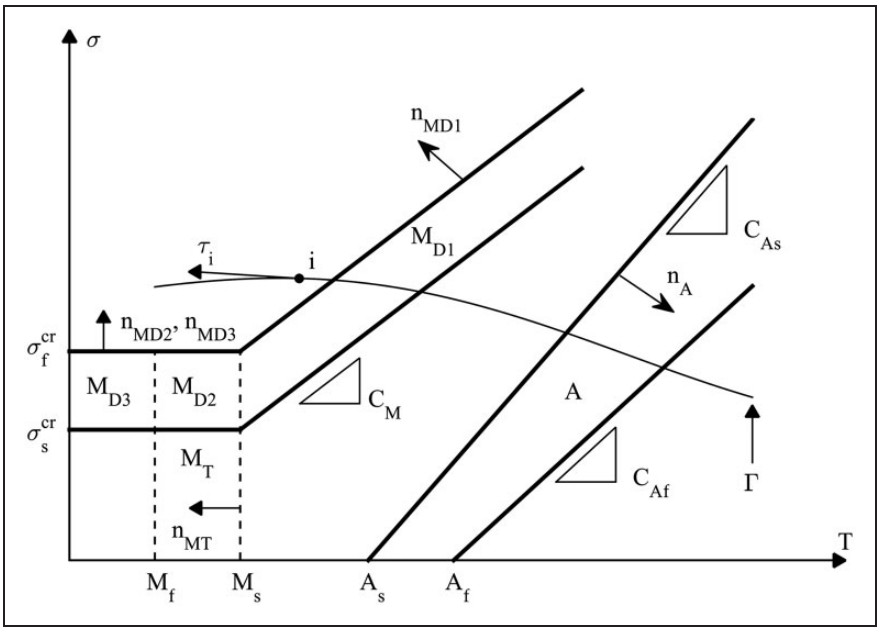

Figure 2. The phase diagram used for the calculation of martensite volume fractions.

function, $f_{i,q}$ can be expressed using the following relations[51]

$$f_{i,s}=\begin{cases}\frac{\xi_{s0}}{2}(Y_A+1) & \text{if } R_k=A\\ \xi_{s0} & \text{if } R_k=M_T\\ \frac{1}{2}\left\{(\xi_{s0}-1)Y_{M_{D1}}+(\xi_{s0}+1)\right\} & \text{if } R_k=M_{D1}\\ \frac{1}{2}\left\{(\xi_{s0}-1)Y_{M_{D23}}+(\xi_{s0}+1)\right\} & \text{if } R_k=M_{D2},M_{D3}\end{cases} \tag{9}$$

$$f_{i,T}=\begin{cases}\frac{\xi_{T0}}{2}(Y_A+1) & \text{if } R_k=A\\ \frac{1-\xi_{s0}-\xi_{T0}}{2}\left(1-Y_{M_T}\right)+\xi_{T0} & \text{if } R_k=M_T\\ \frac{\xi_{T0}}{2}\left(1+Y_{M_{D1}}\right) & \text{if } R_k=M_{D1}\\ \frac{1-\xi_{s0}-\xi_{T0}}{4}\left(1+Y_{M_{D2}}\right)\left(1-Y_{M_T}\right) & \text{if } R_k=M_{D2}\\ \frac{\xi_{T0}}{2}\left(1+Y_{M_{D1}}\right) & \text{if } R_k=M_{D3}\end{cases} \tag{10}$$

in which $Y_A=\cos\left(\pi\frac{(C_{As}(T-A_s)-\tilde{\sigma})}{C_{As}(T-A_s)-C_{Af}(T-A_f)}\right)$, $Y_{M_{D1}}=\cos\left(\pi\frac{\tilde{\sigma}-\sigma_s^{cr}-C_M(T-M_s)}{\sigma_f^{cr}-\sigma_s^{cr}}\right)$, $Y_{M_{D23}}=\cos\left(\pi\frac{\tilde{\sigma}-\sigma_s^{cr}}{\sigma_f^{cr}-\sigma_s^{cr}}\right)$, $Y_{M_T}=\cos\left(\pi\frac{T-M_s}{M_f-M_s}\right)$, and M_f, M_s, A_s, and A_f are martensite finish, martensite start, austenite start, and austenite finish temperatures respectively. C_M, C_{As}, and C_{Af} are the slopes of the transformation bands in the phase diagram as shown in Figure 2.

By applying the principle of complimentary virtual work, the above mentioned 1D constitutive relations can be generalized to 3D one. Considering a unit hemisphere with the surface of Ω and volume of V, one will have

$$\int_V \epsilon_{ij}\delta\sigma_{ij}\mathrm{d}V=\int_\Omega(\epsilon_V\delta\sigma_V+\epsilon_D\delta\sigma_D+\epsilon_T\delta\sigma_T)\mathrm{d}\Omega \tag{11}$$

Substitution equations (1), (2), (4), (5), and (6) into equation (11) followed by simplifications leads to the following relation between macroscopic stress and strain tensors

$$\begin{aligned}\epsilon_{ij}&=-\frac{\nu}{E}\sigma_{rr}\delta_{ij}+\frac{1+\nu}{E}\sigma_{ij}+\frac{3}{2\pi}\epsilon^*\xi_s\int_\Omega\frac{t_in_j+t_jn_i}{2}\mathrm{d}\Omega\\&=\epsilon_{ij}^e+\epsilon_{ij}^{tr}\end{aligned} \tag{12}$$

Note that in this relation the first two terms in the right hand side are associated with the elastic deformation of the material while the last term is associated with the transformation one.

Voigt notation derivation

For the sake of numerical implementation, it is beneficial to explain the constitutive relation expressed by equation (12) using the Voigt notation. Considering the strain and stress vectors as follows

$$\begin{aligned}\mathbf{E}&=\left\{\epsilon_{11}\quad\epsilon_{22}\quad\epsilon_{33}\quad\gamma_{12}\quad\gamma_{13}\quad\gamma_{23}\right\}^{\mathrm{T}}\\&=\left\{\mathrm{E}_1\quad\mathrm{E}_2\quad\mathrm{E}_3\quad\mathrm{E}_4\quad\mathrm{E}_5\quad\mathrm{E}_6\right\}^{\mathrm{T}}\end{aligned} \tag{13}$$

$$\begin{aligned}\mathbf{\Sigma}&=\left\{\sigma_{11}\quad\sigma_{22}\quad\sigma_{33}\quad\sigma_{12}\quad\sigma_{13}\quad\sigma_{23}\right\}^{\mathrm{T}}\\&=\left\{\Sigma_1\quad\Sigma_2\quad\Sigma_3\quad\Sigma_4\quad\Sigma_5\quad\Sigma_6\right\}^{\mathrm{T}}\end{aligned} \tag{14}$$

the Voigt version of the constitutive relation may be explained as

$$\mathrm{E}_i=\frac{1}{E}\beta_i+\frac{3}{2\pi}\epsilon^*\xi_s\int_\Omega\frac{Q_i}{A}\mathrm{d}\Omega,\quad i=1,\ldots,6 \tag{15}$$

in which

$$\beta_i=\begin{cases}(1+\nu)\Sigma_i-\nu\Sigma_m & i\leqslant 3\\ 2(1+\nu)\Sigma_i & i>3\end{cases} \tag{16}$$

$$A^2=\boldsymbol{P}\cdot\hat{\boldsymbol{N}}-(\Sigma_N)^2 \tag{17}$$

$$\boldsymbol{P}=\begin{Bmatrix}\Sigma_1^2+\Sigma_4^2+\Sigma_5^2\\ \Sigma_2^2+\Sigma_4^2+\Sigma_6^2\\ \Sigma_3^2+\Sigma_5^2+\Sigma_6^2\\ \Sigma_4(\Sigma_1+\Sigma_2)+\Sigma_5\Sigma_6\\ \Sigma_5(\Sigma_1+\Sigma_3)+\Sigma_4\Sigma_6\\ \Sigma_6(\Sigma_2+\Sigma_3)+\Sigma_4\Sigma_5\end{Bmatrix} \tag{18}$$

$$\begin{aligned}\boldsymbol{N}&=\left\{N_1\quad N_2\quad N_3\quad N_4\quad N_5\quad N_6\right\}^{\mathrm{T}}\\&=\left\{n_1^2\quad n_2^2\quad n_3^2\quad n_1n_2\quad n_1n_3\quad n_2n_3\right\}^{\mathrm{T}}\end{aligned} \tag{19}$$

$$\hat{\boldsymbol{N}}=\left\{N_1\quad N_2\quad N_3\quad 2N_4\quad 2N_5\quad 2N_6\right\}^{T} \tag{20}$$

$$\Sigma_m=\Sigma_1+\Sigma_2+\Sigma_3 \tag{21}$$

$$\Sigma_N=\mathbf{\Sigma}\cdot\hat{\boldsymbol{N}} \tag{22}$$

$$\boldsymbol{Q}=\boldsymbol{R}-\Sigma_N\hat{\boldsymbol{N}} \tag{23}$$

$$\boldsymbol{R}=\begin{Bmatrix}(\Sigma_1N_1+\Sigma_4N_4+\Sigma_5N_5)\\ (\Sigma_2N_2+\Sigma_4N_4+\Sigma_6N_6)\\ (\Sigma_3N_3+\Sigma_5N_5+\Sigma_6N_6)\\ \Sigma_4(N_1+N_2)+N_4(\Sigma_1+\Sigma_2)+\Sigma_5N_6+\Sigma_6N_5\\ \Sigma_5(N_1+N_3)+N_5(\Sigma_1+\Sigma_3)+\Sigma_4N_6+\Sigma_6N_4\\ \Sigma_6(N_2+N_3)+N_6(\Sigma_2+\Sigma_3)+\Sigma_4N_5+\Sigma_5N_4\end{Bmatrix} \tag{24}$$

In the above relations, $(\cdot)$ denote the dot product operator. Let's define two index generators as follows

$$I(i) = \frac{1}{2}\left[9 + i + \frac{1+(-1)^i}{2}\right] \tag{25}$$

$$J(i) = \frac{1}{2}\left[7 + i - \frac{1+(-1)^i}{2}\right] \tag{26}$$

Using these two index generators, the vectors $\boldsymbol{P}$ and $\boldsymbol{R}$ can be expressed in the index format as

$$P_i = \begin{cases} \sigma_i^2 + \sigma_{I(i)}^2 + \sigma_{J(i)}^2 & i \leqslant 3 \\ \sigma_i\left(\sigma_{I(i-3)-3} + \sigma_{J(i-3)-3}\right) + \sigma_{I(7-i)}\sigma_{J(7-i)} & i > 3 \end{cases} \tag{27}$$

$$R_i = \begin{cases} \Sigma_i N_i + \Sigma_{I(i)} N_{I(i)} + \Sigma_{J(i)} N_{J(i)} & i \leqslant 3 \\ \left\{ \begin{array}{c} \Sigma_i\left(N_{I(i-3)-3} + N_{J(i-3)-3}\right) \\ +N_i\left(\Sigma_{I(i-3)-3} + \Sigma_{J(i-3)-3}\right) \\ +\Sigma_{I(7-i)} N_{J(7-i)} + N_{I(7-i)}\Sigma_{J(7-i)} \end{array} \right\} & i > 3 \end{cases} \tag{28}$$

Numerical implementation

In this section, first the incremental derivation of the constitutive model is presented for the sake of numerical implementations. Then, the numerical integration over the surface of a hemisphere is presented. Finally, the numerical method utilized for inversion of the arisen matrix is explained.

Incremental form

In order to implement a constitutive model through the user material subroutine, UMAT, in ABAQUS finite element package, it is necessary to explain the stress increment vector, $\Delta\boldsymbol{\Sigma}$, as a function of the strain increment vector, $\Delta\mathbf{E}$. To do so, the following relation is utilized

$$\Delta \mathrm{E}_i = \sum_{j=1}^{6} \frac{\partial \mathrm{E}_i}{\partial \Sigma_j} \Delta\Sigma_j + \frac{\partial \mathrm{E}_i}{\partial T} \Delta T \tag{29}$$

where (∂) denotes the partial differentiation. From the computational point of view, $\left(\frac{\partial \mathrm{E}_i}{\partial \Sigma_j}\right)^{-1}$ will be served as the continuum tangent stiffness matrix and $\left(\frac{\partial \mathrm{E}_i}{\partial \Sigma_j}\right)^{-1}\left(\frac{\partial \mathrm{E}_i}{\partial T}\right)$ the tangent thermal moduli vector. Differentiating equation (15) yields the two following relations

$$\frac{\partial \mathrm{E}_i}{\partial \Sigma_j} = C_{ij} = C_{ij}^{e(1)} + C_{ij}^{e(2)} + C_{ij}^{tr(1)} + C_{ij}^{tr(2)} \tag{30}$$

$$\frac{\partial \mathrm{E}_i}{\partial T} = \begin{cases} \left\{ \begin{array}{c} \left(\frac{1}{E_M} - \frac{1}{E_A}\right)\frac{\partial \xi}{\partial T}\left[(1+\nu)\Sigma_i - \nu\Sigma_m\right] \\ +\frac{3}{4\pi}\epsilon^* \frac{\partial \xi_s}{\partial T}\int_\Omega \frac{Q_i}{A}\,\mathrm{d}\Omega \end{array} \right\} & i \leqslant 3 \\ 2\left(\frac{1}{E_M} - \frac{1}{E_A}\right)\frac{\partial \xi}{\partial T}(1+\nu)\Sigma_i + \frac{3}{2\pi}\epsilon^* \frac{\partial \xi_s}{\partial T}\int_\Omega \frac{Q_i}{A}\,\mathrm{d}\Omega & i > 3 \end{cases} \tag{31}$$

in which

$$\boldsymbol{C}^{e(1)} = \frac{1}{E}\begin{bmatrix} 1 & -\nu & -\nu & 0 & 0 & 0 \\ -\nu & 1 & -\nu & 0 & 0 & 0 \\ -\nu & -\nu & 1 & 0 & 0 & 0 \\ 0 & 0 & 0 & 2(1+\nu) & 0 & 0 \\ 0 & 0 & 0 & 0 & 2(1+\nu) & 0 \\ 0 & 0 & 0 & 0 & 0 & 2(1+\nu) \end{bmatrix} \tag{32}$$

$$C_{ij}^{e(2)} = \begin{cases} \frac{1}{2\bar{\sigma}}\beta_i\left(3\Sigma_j - \Sigma_m\right)\left(\frac{1}{E_M} - \frac{1}{E_A}\right)\frac{\partial \bar{\xi}}{\partial \bar{\sigma}} & j \leqslant 3 \\ \frac{3}{\bar{\sigma}}\beta_i\Sigma_j\left(\frac{1}{E_M} - \frac{1}{E_A}\right)\frac{\partial \bar{\xi}}{\partial \bar{\sigma}} & j > 3 \end{cases} \tag{33}$$

$$C_{ij}^{tr(1)} = \frac{3}{2\pi\bar{\sigma}}\epsilon^* \frac{\partial \xi_s}{\partial \bar{\sigma}} \begin{cases} \int_\Omega \frac{Q_i}{2A}\left(3\Sigma_j - \Sigma_m\right) & j \leqslant 3 \\ \int_\Omega \frac{3Q_i}{A}\Sigma_j & j < 3 \end{cases} \tag{34}$$

$$C_{ij}^{tr(2)} = \frac{3}{2\pi}\epsilon^* \xi_s \int_\Omega \frac{1}{A}\left(\frac{\partial Q_i}{\partial \Sigma_j} - \frac{Q_i}{A}\frac{\partial A}{\partial \Sigma_j}\right)\mathrm{d}\Omega \tag{35}$$

$$\frac{\partial Q_i}{\partial \Sigma_j} = \begin{bmatrix} N_1(1-N_1) & -N_1N_2 & -N_1N_3 & N_4(1-2N_1) & N_5(1-2N_1) & -2N_1N_6 \\ -N_1N_2 & N_2(1-N_2) & -N_2N_3 & N_4(1-2N_2) & -2N_2N_5 & N_6(1-2N_2) \\ -N_1N_3 & -N_2N_3 & N_3(1-N_3) & -2N_3N_4 & N_5(1-2N_3) & N_6(1-2N_3) \\ N_4(1-2N_1) & N_4(1-2N_2) & -2N_3N_4 & N_1+N_2-4N_4^2 & N_6-4N_4N_5 & N_5-4N_4N_6 \\ N_5(1-2N_1) & -2N_2N_5 & N_5(1-2N_3) & N_6-4N_4N_5 & N_1+N_3-4N_5^2 & N_4-4N_5N_6 \\ -2N_1N_6 & N_6(1-2N_2) & N_6(1-2N_3) & N_5-4N_4N_6 & N_4-4N_5N_6 & N_2+N_3-4N_6^2 \end{bmatrix} \tag{36}$$

$$\frac{\partial A}{\partial \boldsymbol{\Sigma}} = \frac{1}{A}\begin{Bmatrix} (\Sigma_1 N_1 + \Sigma_4 N_4 + \Sigma_5 N_5 - N_1 \Sigma_N) \\ (\Sigma_2 N_2 + \Sigma_4 N_4 + \Sigma_6 N_6 - N_2 \Sigma_N) \\ (\Sigma_3 N_3 + \Sigma_5 N_5 + \Sigma_6 N_6 - N_3 \Sigma_N) \\ \Sigma_4(N_1 + N_2) + N_4(\Sigma_1 + \Sigma_2) + \Sigma_5 N_6 + \Sigma_6 N_5 - 2N_4 \Sigma_N \\ \Sigma_5(N_1 + N_3) + N_5(\Sigma_1 + \Sigma_3) + \Sigma_4 N_6 + \Sigma_6 N_4 - 2N_5 \Sigma_N \\ \Sigma_6(N_2 + N_3) + N_6(\Sigma_2 + \Sigma_3) + \Sigma_4 N_5 + \Sigma_5 N_4 - 2N_6 \Sigma_N \end{Bmatrix} \tag{37}$$

To be able to assess the effects of the increment size in the forward Euler implementation scheme, the following incremental integration is utilized

$$\boldsymbol{\Sigma}^{(n+1)} = \boldsymbol{\Sigma}^{(n)} + \Delta\boldsymbol{\Sigma}^{(n)} = \boldsymbol{\Sigma}^{(n)} + \left(\boldsymbol{C}^{(n)}\right)^{-1}\left(\Delta \mathbf{E}^{(n)} - \frac{\partial \mathbf{E}^{(n)}}{\partial T}\Delta T\right) \tag{38}$$

Numerical integration over the surface of unit hemisphere

Referring to equations (15), (31), (34), and (35), it is necessary to calculate some integrals over the surface of a hemisphere. Since the functions to be integrated have no exact integral solutions, a numerical method must be utilized in this regard. To do so, the numerical integration method proposed by Bazant and Oh[52] is used in this paper. Considering $f(x_1, x_2, x_3)$ as the function to be integrated, the integral over the surface of a hemisphere may be approximated by the following relation

$$\int_{\Omega} f(x_1, x_2, x_3)\mathrm{d}\Omega = \sum_{k=1}^{M} w_k f\left(\zeta_1^k, \zeta_2^k, \zeta_3^k\right) \tag{39}$$

in which w_k are weights and ζ_1^k, ζ_2^k, ζ_3^k the direction cosines. In this paper, five different integration formulas including orthogonal symmetry 2*21 points, O21, orthogonal symmetry 2*33 points, O33, orthogonal symmetry 37 points, O37, no orthogonal symmetry 2*21 points, NO21, and no orthogonal symmetry 2*61 points, NO61, are utilized for numerical integration.[52,53] The weights and direction cosines for these formulations are presented in Appendix.

Matrix inversion

Referring to equation (38), in each increment, it is necessary to obtain the inverse of $\boldsymbol{C}^{(n)}$, a 6*6 matrix. Every numerical inversion technique may be used for this purpose. However, in this paper, an iterative numerical approach with seventh-order convergence is utilized for finding the inverse. Suppose that the inverse of $\boldsymbol{B} \in \mathbb{C}^{m\times m}$ is going to be calculated. Based on what proposed by Soleymani,[54] the following iterative method can be used

$$\begin{aligned} \boldsymbol{V}_{n+1} = \boldsymbol{V}_n(7\boldsymbol{I} + \boldsymbol{B}\boldsymbol{V}_n(-21\boldsymbol{I} + \boldsymbol{B}\boldsymbol{V}_n(35\boldsymbol{I} + \boldsymbol{B}\boldsymbol{V}_n(-35\boldsymbol{I} \\ + \boldsymbol{B}\boldsymbol{V}_n(21\boldsymbol{I} + \boldsymbol{B}\boldsymbol{V}_n(-7\boldsymbol{I} + \boldsymbol{B}\boldsymbol{V}_n)))))) \end{aligned} \tag{40}$$

The matrix $\boldsymbol{V}$ will converge to the inverse of $\boldsymbol{B}$, if a suitable initial approximation, $\boldsymbol{V}_0$, is chosen. It has been previously proposed that the following initial guess will lead to a good convergence[54]

$$\boldsymbol{V}_0 = \frac{\boldsymbol{B}^T}{\|\boldsymbol{B}\|_1 \|\boldsymbol{B}\|_\infty} \tag{41}$$

where subscript T stands for transpose, $\|\boldsymbol{B}\|_1 = \max_{\mathrm{j}}\left(\sum_{i=1}^{m}|b_{ij}|\right)$, and $\|\boldsymbol{B}\|_\infty = \max_{i}\left(\sum_{j=1}^{m}|b_{ij}|\right)$.

Results and discussion

In this section, the numerically implemented constitutive model is examined and the effects of stress increment size, integration formula, loading direction, and different load cases are investigated. In all the cases, the hypothetical material parameters presented in Table 1 are utilized for modeling purposes. Note that in the case of superelastic regime, the initial values of stress- and temperature-induced martensite are both zero and the temperature is supposed to be 60 °C. For shape memory response of SMA, the initial value of stress-induced martensite volume fraction is zero while the initial value of temperature-induced one is one.

Table 1. Material parameters used for modeling purposes.

E_A (MPa)	E_M(MPa)	ν	M_f (°C)	M_s (°C)	A_s (°C)	A_f (°C)
60000	40000	0.3	10	20	40	50
σ_s^{cr} (MPa)	σ_f^{cr} (MPa)	$C_M\left(\frac{\text{MPa}}{^\circ\text{C}}\right)$	$C_{As}\left(\frac{\text{MPa}}{^\circ\text{C}}\right)$	$C_{Af}\left(\frac{\text{MPa}}{^\circ\text{C}}\right)$	ϵ^*	
50	150	5	8	7	0.025	

The initial temperature is supposed to be 0 °C, then it is heated up to 60 °C, and again cooled down to 0 °C.

Effect of stress increment size

As stated before, in this paper, the presented constitutive model is implemented using forward Euler to be able to assess the sensitivity of the model to the increment size. Figure 3 shows the effects of different stress increments on the uniaxial stress–strain response of SMA obtained using O21 integration formula.

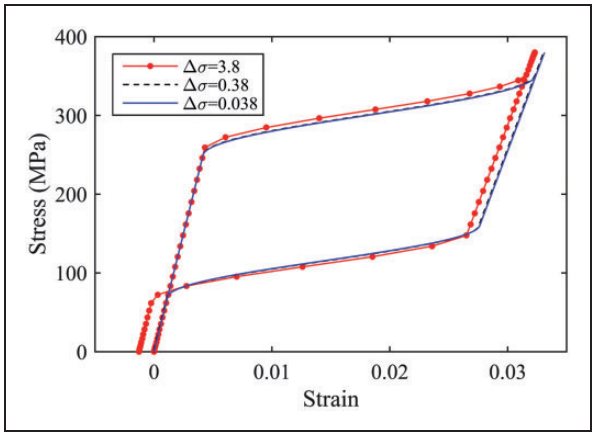

Figure 3. The effect of the stress increment size on the stress–strain response of SMAs in the superelastic regime.

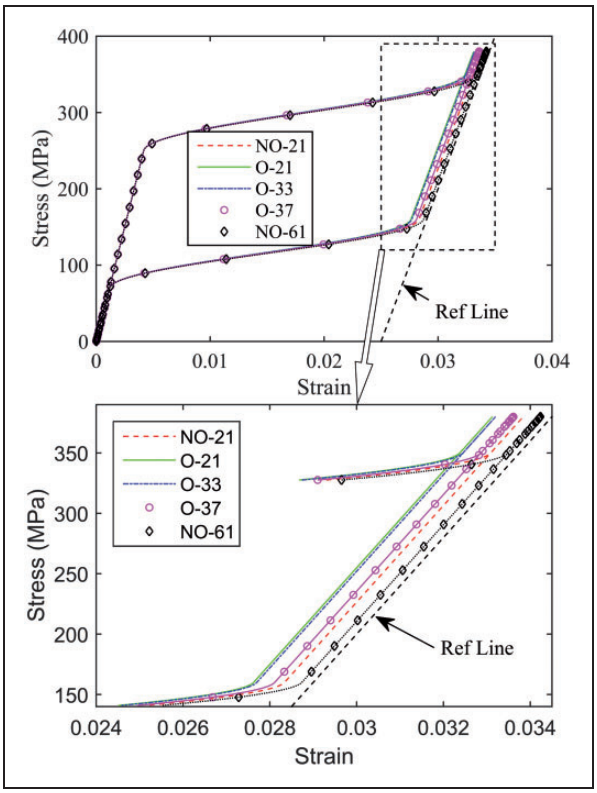

Figure 4. The effects of different integration formulas on the uniaxial stress–strain response of SMA loaded in x_1 direction.

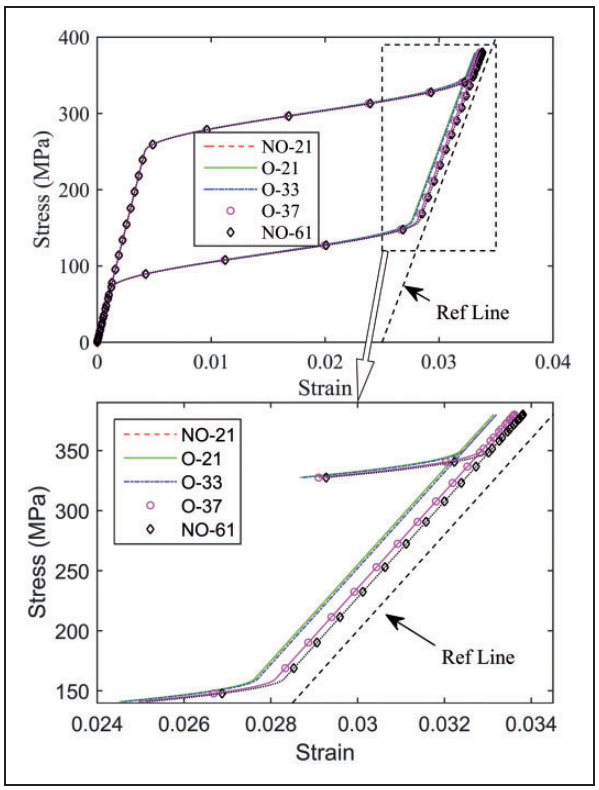

Figure 5. The effects of different integration formulas on the uniaxial stress–strain response of SMA loaded in x_2 direction.

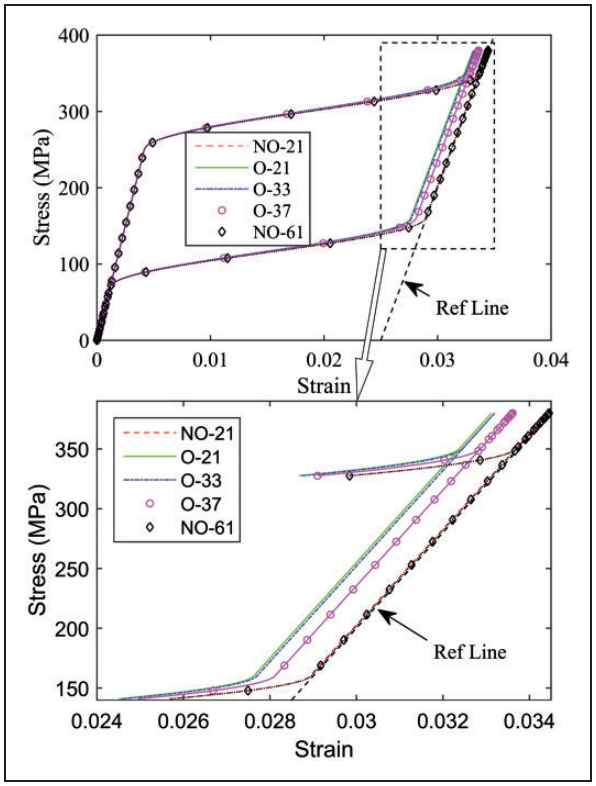

Figure 6. The effects of different integration formulas on the uniaxial stress–strain response of SMA loaded in x_3 direction.

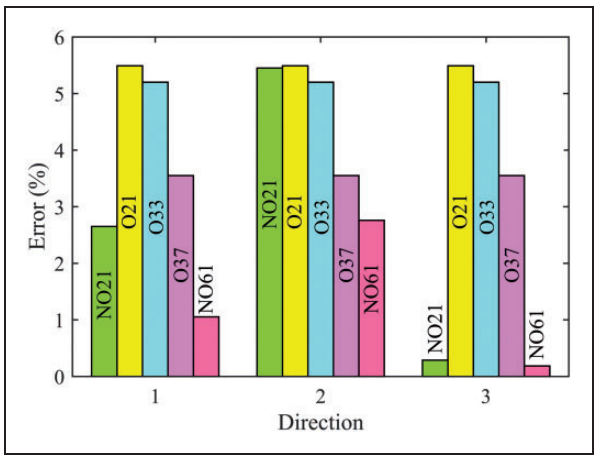

Figure 7. The error of the predicted value of maximum recoverable strain with its exact value.

As can be seen, large stress increments may yield to inaccurate results due to forward Euler integration scheme. Accordingly, sufficiently small stress increments are required to be able to achieve desirable results. It is worth mentioning that the same results can be obtained using the other integration formula but the results are not presented here for the sake of brevity. In the rest of this paper, a sufficiently small stress increment is utilized to be sure about the accuracy of the results.

Effects of integration formula and loading direction

In this section, the effects of different integration formulas and loading direction are investigated for different load cases including uniaxial, pure shear, and nonproportional tension-torsion.

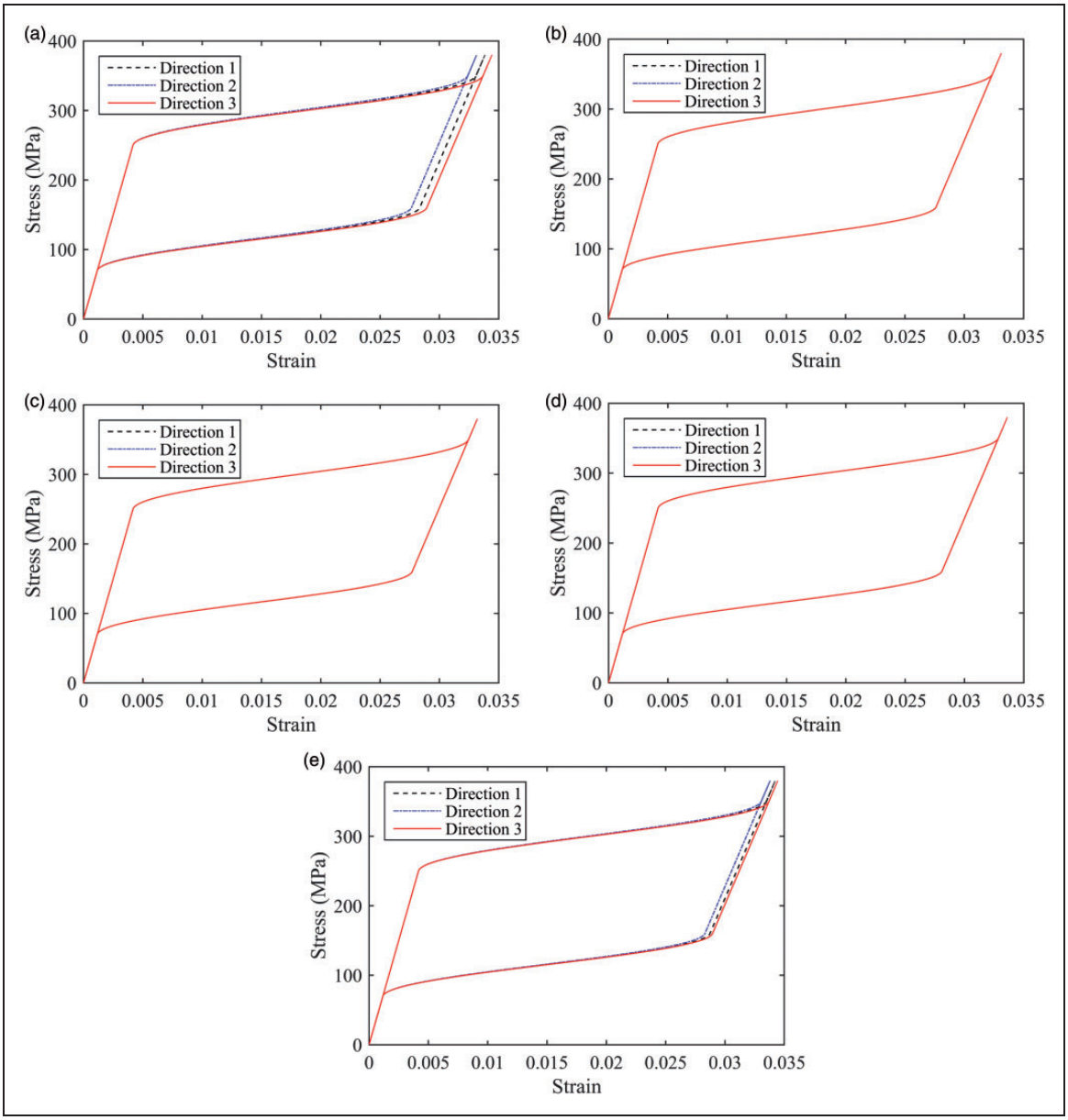

Figure 8. Comparison of the stress–strain response loaded in different directions for: (a) NO21, (b) O21, (c) O33, (d) O37, and (e) NO61.

Uniaxial loading. Figures 4 to 6 show the uniaxial superelastic stress–strain response of SMA loaded in x_1, x_2, and x_3 directions respectively. Based on the exact solution of uniaxial loading–unloading response of SMA, the first linear portion of the unloading response must coincide with the dashed line indicated as ''Ref Line''. In other words, the continuation of this linear portion must pass through the maximum recoverable strain, ϵ^*. According to these figures, in all the cases, the predicted maximum recoverable strain is smaller than the exact value. Figure 7 compares the error of predicted maximum recoverable strain with the exact value for different integration formulas and different loading directions. Referring to this figure, for all loading directions, the minimum error is associated with the NO61 integration formula while the maximum error is related to the O21 one.

Figure 8(a) to (e) compares the stress–strain response of SMA loaded in different directions for NO21, O21, O33, O37, and NO61 integration formulas respectively. Since the material is isotropic, the stress–strain curves of all the loading directions must be coincided. But for NO21 and NO61 the curves are not coincided because of not being orthogonally symmetric. However, for O21, O33, and O37 the stress–strain response is similar for all the loading directions due to the orthogonal symmetry of these formulations. Notice that the level of anisotropy predicted by NO61 integration formula is smaller than that of NO21 because of the higher accuracy of the former.

The stress–strain-temperature response of SMA in shape memory regime obtained using O21 integration formula is depicted in Figure 9. The material, which is initially free of stress in the twinned martensite state, is loaded uniaxially at a constant temperature until it is converted to detwinned martensite, and then unloaded to zero stress state. After that, at a constant stress, the material is heated up to $T = 60\,^{\circ}\mathrm{C}$ and cooled down to $T = 0\,^{\circ}\mathrm{C}$. As it can be seen from this figure, the residual strain upon cooling is too small meaning shape memory effect. It is worthwhile to mention that the same behavior is observed for all the integration formulas (not presented here for the sake of brevity). Figure 10 shows the stress-strain curve in the shape memory regime obtained using different integration formulas. As shown in this figure, the predicted maximum recoverable strain is not coincided with the exact value. Again, the maximum error is associated with O21 integration formula while the minimum error is related to O61 one. Referring to Figures 9 and 10, it can be concluded that although the prediction of the maximum recoverable strain contains a pronounced value of error, the predicted residual strain show a very small error with its exact value (zero). Referring to equation (29), it is obvious that during the thermal loading of the material, the stress increment is zero. Accordingly, the first term of the right hand side of this equation would be zero too. So, the error of the thermal loading portion of the curve is associated with the second term which is very small leading to a small deviation from the exact value of the residual strain upon cooling.

Pure shear. Figures 11 to 13 show the stress–strain response of SMA under pure shear for 12, 13, and 23 components respectively. Similar to that observed for uniaxial loading of SMA, in the pure shear loading, due to the errors of the numerical integration formulas, the predicted maximum recoverable strain is not equal to the exact value which is $\sqrt{3}\epsilon^*$. As

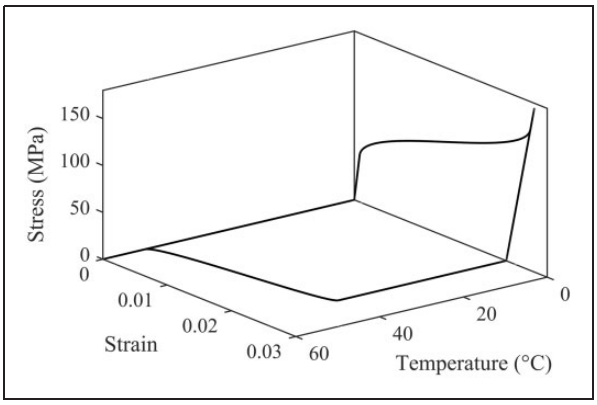

Figure 9. The stress–strain–temperature response of SMA in shape memory regime obtained using O21 integration formula.

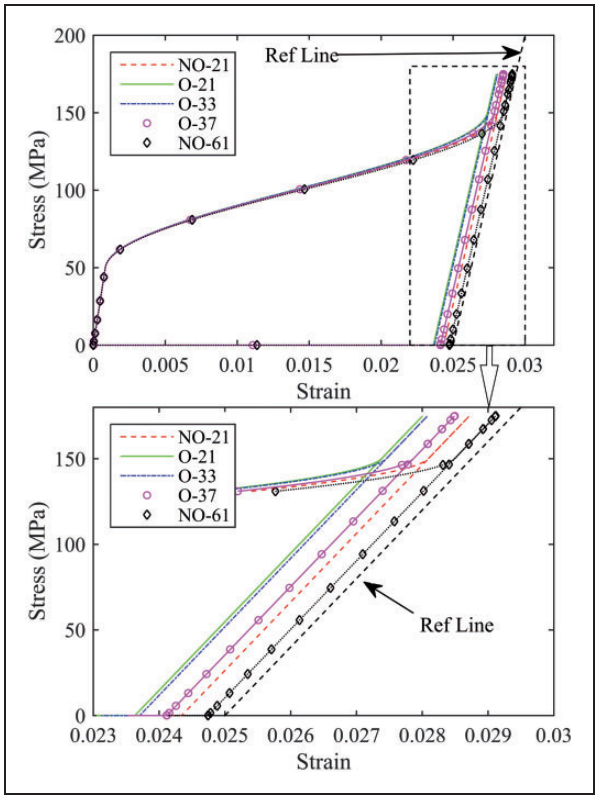

Figure 10. Stress–strain response of SMA in shape memory regime obtained using different integration formulas.

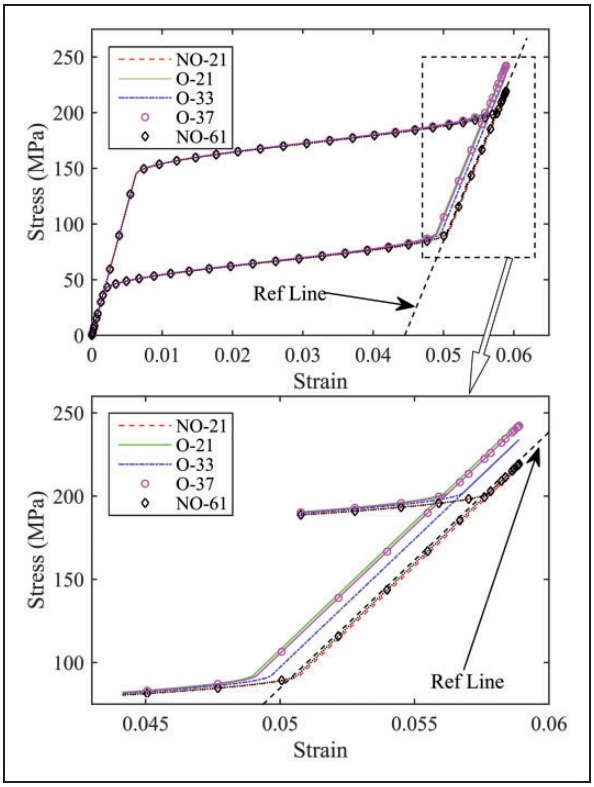

Figure 11. The effects of different integration formulas on the $\tau_{12} - \gamma_{12}$ response of SMA in pure shear mode.

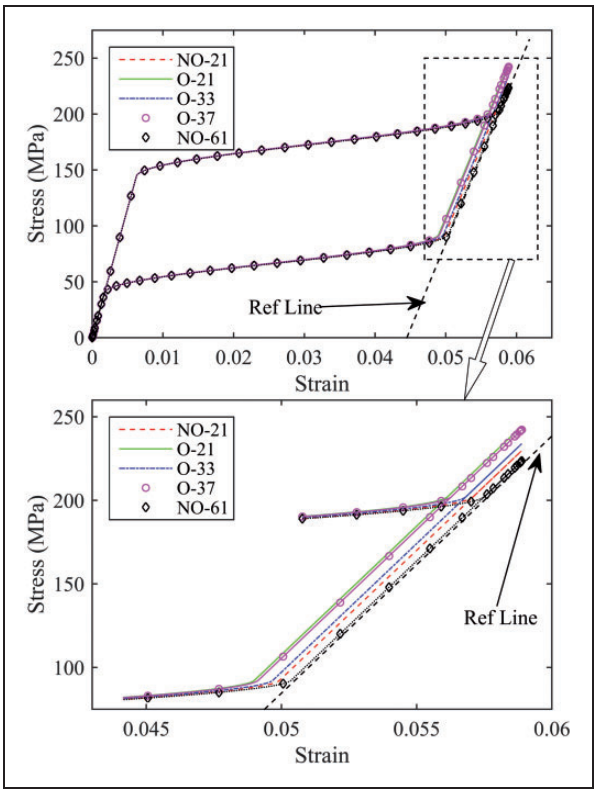

Figure 12. The effects of different integration formulas on the $\tau_{13} - \gamma_{13}$ response of SMA in pure shear mode.

shown in Figure 14, the maximum and minimum errors with the exact value are respectively associated with O21 and NO61 integration formulas that is similar to that observed for uniaxial loading.

Nonproportional loading. To complete this section, the square shaped non-proportional strain control loading shown in Figure 15(a) is simulated. The corresponding stress response of this loading condition obtained using NO21, NO61, O37, and O33 integration formulas is presented in Figure 15(b). As can be

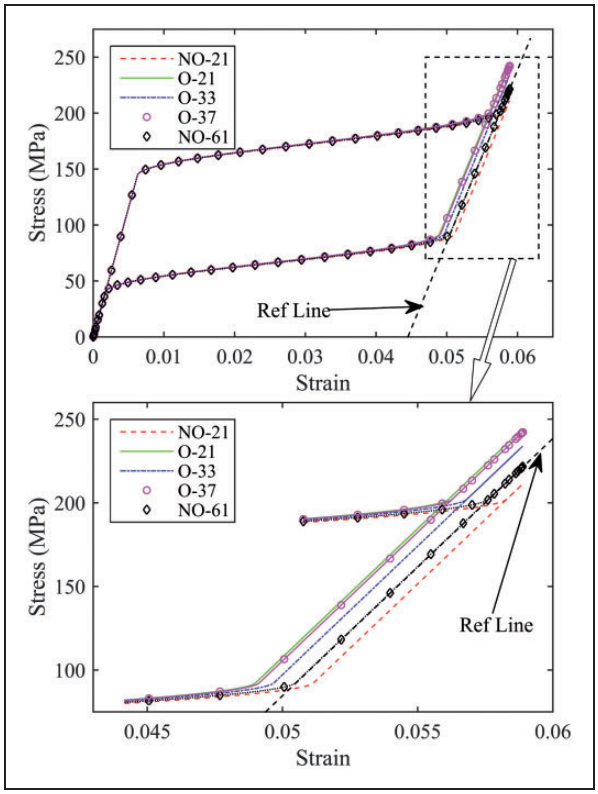

Figure 13. The effects of different integration formulas on the $\tau_{23} - \gamma_{23}$ response of SMA in pure shear mode.

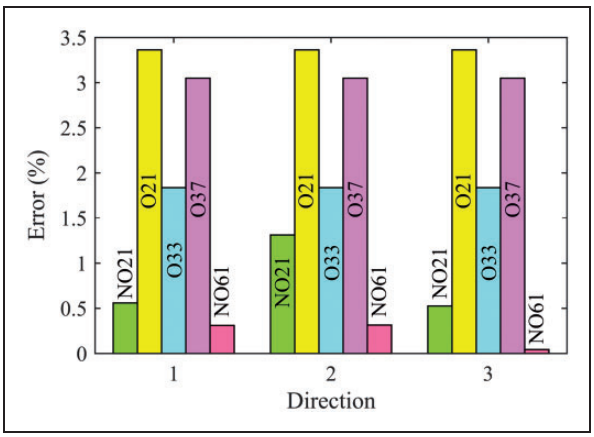

Figure 14. The error of the predicted value of maximum recoverable strain in pure shear with its exact value.

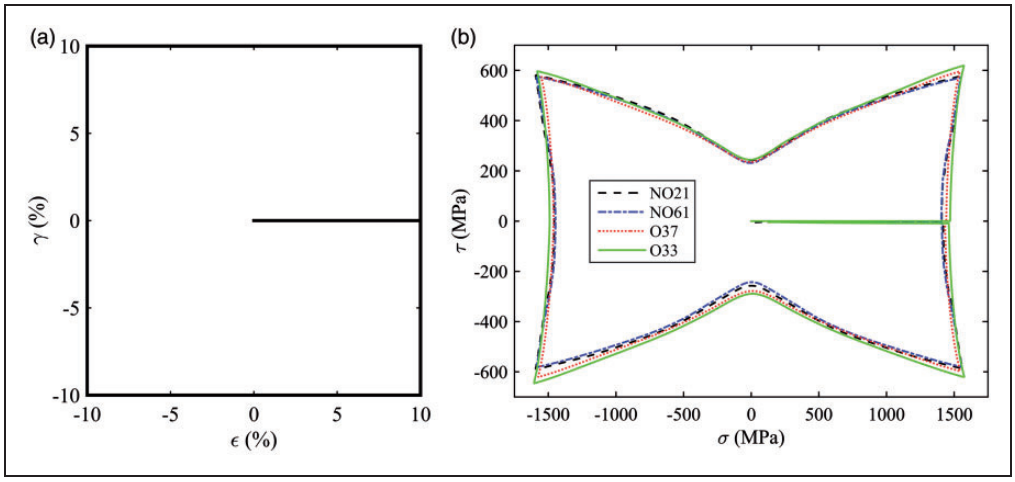

Figure 15. (a) The square-shaped nonproportional strain control loading; (b) the corresponding stress output.

seen, the shear stress–normal stress response obtained using all integration formulas is near each other. However, referring to the previous subsections, accepting NO61 as the most accurate one, it can be concluded that the accuracy of NO21 is higher than O37 and O33. In addition, the results show that the two formulas with orthogonal symmetry provide similar results. This is also true for both the formulas without orthogonal symmetry.

Conclusion

In this paper, an existing constitutive model based on microplane theory is numerically implemented through finite element method. To do so, first the basic relations of the model are derived in tensorial form. Then, the Voigt notation of the tensorial formulation is explained for the sake of numerical implementation. After that, the numerical implementation procedure including incremental formulation, numerical integration over the surface of a unit sphere, and numerical inversion of the arising matrix is presented. Finally, the effects of stress increment size, different numerical integration formulas, and loading direction is investigated through superelastic and shape memory proportional and nonproportional loadings. The results show that in all cases, the NO61 scheme provides the most accurate results while O21 scheme is the most inaccurate integration formula. However, the two integration formulas without orthogonal symmetry show a little anisotropy while the three orthogonally symmetric formulas provide isotropic response of SMA.

Declaration of conflicting interests

The author(s) declared no potential conflicts of interest with respect to the research, authorship, and/or publication of this article.

Funding

The author(s) received no financial support for the research, authorship, and/or publication of this article.

References

1. Buehler WJ, Gilfrich J and Wiley R. Effect of low-temperature phase changes on the mechanical properties of alloys near composition TiNi. *J Appl Phys* 1963; 34: 1475–1477.
2. Andani MT, Saedi S, Turabi AS, et al. Mechanical and shape memory properties of porous Ni 50.1 Ti 49.9 alloys manufactured by selective laser melting. *J Mech Behav Biomed Mater* 2017; 68: 224–231.
3. Auricchio F and Petrini L. A three-dimensional model describing stress-temperature induced solid phase transformations: solution algorithm and boundary value problems. *Int J Numer Meth Eng* 2004; 61: 807–836.
4. Auricchio F and Taylor RL. Shape-memory alloys: Modelling and numerical simulations of the finite-strain superelastic behavior. *Comput Meth Appl Mech Eng* 1997; 143: 175–194.
5. Bouvet C, Calloch S and Lexcellent C. A phenomenological model for pseudoelasticity of shape memory alloys under multiaxial proportional and nonproportional loadings. *Eur J Mech-A/Solids* 2004; 23: 37–61.
6. Lagoudas DC, Entchev PB, Popov P, et al. Shape memory alloys, Part II: Modeling of polycrystals. *Mech Mater* 2006; 38: 430–462.
7. Paiva A, Savi MA, Braga AMB, et al. A constitutive model for shape memory alloys considering tensile–compressive asymmetry and plasticity. *Int J Solids Struct* 2005; 42: 3439–3457.
8. Qidwai M and Lagoudas D. On thermomechanics and transformation surfaces of polycrystalline NiTi shape memory alloy material. *Int J Plast* 2000; 16: 1309–1343.
9. Saint-Sulpice L, Chirani SA and Calloch S. A 3D superelastic model for shape memory alloys taking into account progressive strain under cyclic loadings. *Mech Mater* 2009; 41: 12–26.
10. Yu C, Kang G, Kan Q, et al. A micromechanical constitutive model based on crystal plasticity for thermomechanical cyclic deformation of NiTi shape memory alloys. *Int J Plast* 2013; 44: 161–191.
11. Karamooz, Ravari MR, Kadkhodaei M and Ghaei A. A microplane constitutive model for shape memory alloys considering tension–compression asymmetry. *Smart Mater Struct* 2015; 24: 075016.

12. Auricchio F, Reali A and Stefanelli U. A macroscopic 1D model for shape memory alloys including asymmetric behaviors and transformation-dependent elastic properties. *Comput Meth Appl Mech Eng* 2009; 198: 1631–1637.
13. Feng X-Q and Sun Q. Shakedown analysis of shape memory alloy structures. *Int J Plast* 2007; 23: 183–206.
14. Grabe C and Bruhns OT. On the viscous and strain rate dependent behavior of polycrystalline NiTi. *Int J Solids Struct* 2008; 45: 1876–1895.
15. Morin C, Moumni Z and Zaki W. A constitutive model for shape memory alloys accounting for thermomechanical coupling. *Int J Plast* 2011; 27: 748–767.
16. Morin C, Moumni Z and Zaki W. Thermomechanical coupling in shape memory alloys under cyclic loadings: Experimental analysis and constitutive modeling. *Int J Plast* 2011; 27: 1959–1980.
17. Cisse C, Zaki W and Zineb TB. A review of constitutive models and modeling techniques for shape memory alloys. *Int J Plast* 2016; 76: 244–284.
18. Bhattacharya K and Kohn RV. Symmetry, texture and the recoverable strain of shape-memory polycrystals. *Acta Mater* 1996; 44: 529–542.
19. Lu Z and Weng G. Martensitic transformation and stress-strain relations of shape-memory alloys. *J Mech Phys Solids* 1997; 45: 1905–1928.
20. Lu Z and Weng G. A self-consistent model for the stress–strain behavior of shape-memory alloy polycrystals. *Acta Mater* 1998; 46: 5423–5433.
21. Reese S and Christ D. Finite deformation pseudo-elasticity of shape memory alloys–Constitutive modelling and finite element implementation. *Int J Plast* 2008; 24: 455–482.
22. Sun QP and Hwang KC. Micromechanics modelling for the constitutive behavior of polycrystalline shape memory alloys—I. Derivation of general relations. *J Mech Phys Solids* 1993; 41: 1–17.
23. Arghavani J, Auricchio F, Naghdabadi R, et al. A 3-D phenomenological constitutive model for shape memory alloys under multiaxial loadings. *Int J Plast* 2010; 26: 976–991.
24. Arghavani J, Auricchio F and Naghdabadi R. A finite strain kinematic hardening constitutive model based on Hencky strain: General framework, solution algorithm and application to shape memory alloys. *Int J Plast* 2011; 27: 940–961.
25. Chemisky Y, Chatzigeorgiou G, Kumar P, et al. A constitutive model for cyclic actuation of high-temperature shape memory alloys. *Mech Mater* 2014; 68: 120–136.
26. Chemisky Y, Duval A, Patoor E, et al. Constitutive model for shape memory alloys including phase transformation, martensitic reorientation and twins accommodation. *Mech Mater* 2011; 43: 361–376.
27. Panico M and Brinson L. A three-dimensional phenomenological model for martensite reorientation in shape memory alloys. *J Mech Phys Solids* 2007; 55: 2491–2511.
28. Sedlak P, Frost M, Benešová B, et al. Thermomechanical model for NiTi-based shape memory alloys including R-phase and material anisotropy under multi-axial loadings. *Int J Plast* 2012; 39: 132–151.
29. Thamburaja P. A finite-deformation-based phenomenological theory for shape-memory alloys. *Int J Plast* 2010; 26: 1195–1219.
30. Xiao H. An explicit, straightforward approach to modeling SMA pseudoelastic hysteresis. *Int J Plast* 2014; 53: 228–240.
31. Yu C, Kang G and Kan Q. Study on the rate-dependent cyclic deformation of super-elastic NiTi shape memory alloy based on a new crystal plasticity constitutive model. *Int J Solids Struct* 2014; 51: 4386–4405.
32. Yu C, Kang G, Song D, et al. Effect of martensite reorientation and reorientation-induced plasticity on multiaxial transformation ratchetting of super-elastic NiTi shape memory alloy: New consideration in constitutive model. *Int J Plast* 2015; 67: 69–101.
33. Yu C, Kang G and Kan Q. Crystal plasticity based constitutive model of NiTi shape memory alloy considering different mechanisms of inelastic deformation. *Int J Plast* 2014; 54: 132–162.
34. Scalet G. Shape memory and elastoplastic materials: from constitutive and numerical to fatigue modeling. Alma, 2014.
35. Qidwai M and Lagoudas D. Numerical implementation of a shape memory alloy thermomechanical constitutive model using return mapping algorithms. *Int J Numer Meth Eng* 2000; 47: 1123–1168.
36. Arghavani J, Auricchio F, Naghdabadi R, et al. On the constitutive modeling and numerical implementation of shape memory alloys under multiaxial loadings-Part I: Constitutive model development at small and finite strains. In: *Proceedings of the school and symposium on smart structural systems technologies, Keynote Lecture*, Porto, 5–9 April 2010.
37. Arghavani J, Auricchio F, Naghdabadi R, et al. On the constitutive modeling and numerical implementation of shape memory alloys under multiaxial loadings-Part II: Numerical implementation and simulations. In: *Proceedings of the school and symposium on smart structural systems technologies*, Porto, 5–9 April 2010.
38. Wang X, Xu B and Yue Z. Micromechanical modelling of the effect of plastic deformation on the mechanical behaviour in pseudoelastic shape memory alloys. *Int J Plast* 2008; 24: 1307–1332.
39. Hartl D and Lagoudas D. Constitutive modeling and structural analysis considering simultaneous phase transformation and plastic yield in shape memory alloys. *Smart Mater Struct* 2009; 18: 104017.
40. Stebner A and Brinson L. Explicit finite element implementation of an improved three dimensional constitutive model for shape memory alloys. *Comput Meth Appl Mech Eng* 2013; 257: 17–35.
41. Auricchio F, Bonetti E, Scalet G, et al. Theoretical and numerical modeling of shape memory alloys accounting for multiple phase transformations and martensite reorientation. *Int J Plast* 2014; 59: 30–54.
42. Karamooz Ravari MR. *Constitutive modeling of cellular shape memory alloys using microplane method*. PhD Thesis, Isfahan University of Technology, Iran, 2015.
43. Brocca M, Brinson LC and Bažant ZP. Three-dimensional constitutive model for shape memory

alloys based on microplane model. *J Mech Phys Solids* 2002; 50: 1051–1077.
44. Kadkhodaei M, Salimi M, Rajapakse R, et al. Microplane modelling of shape memory alloys. *Phys Scripta* 2007; 2007: 329.
45. Kadkhodaei M, Salimi MH, Rajapakse R, et al. Modeling of shape memory alloys based on microplane theory. *J Intell Mater Syst Struct* 2007.
46. Mehrabi R, Kadkhodaei M and Elahinia M. A thermodynamically-consistent microplane model for shape memory alloys. *Int J Solids Struct* 2014; 51: 2666–2675.
47. Mehrabi R and Ravari MRK. Simulation of superelastic SMA helical springs. *Smart Struct Syst* 2015; 16: 183–194.
48. Karamooz Ravari MR, Esfahani SN, Andani MT, et al. On the effects of geometry, defects, and material asymmetry on the mechanical response of shape memory alloy cellular lattice structures. *Smart Mater Struct* 2016; 25: 025008.
49. Karamooz Ravari MR, Kadkhodaei M and Ghaei A. Effects of asymmetric material response on the mechanical behavior of porous shape memory alloys. *J Intell Mater Syst Struct* 2015.
50. Karamooz Ravari MR, Kadkhodaei M and Ghaei A. A unit cell model for simulating the stress-strain response of porous shape memory alloys. *J Mater Eng Perform* 2015; 24: 4096–4105.
51. Poorasadion S, Arghavani J, Naghdabadi R, et al. An improvement on the Brinson model for shape memory alloys with application to two-dimensional beam element. *J Intell Mater Syst Struct* 2013; DOI: 1045389X13512187.
52. Bažant P and Oh B. Efficient numerical integration on the surface of a sphere. *ZAMM. J Appl Math Mech* 1986; 66: 37–49.
53. Bazant ZP and Oh BH. Microplane model for progressive fracture of concrete and rock. *J Eng Mech* 1985; 111: 559–582.
54. Soleymani F. On a fast iterative method for approximate inverse of matrices. *Commun Korean Math Soc* 2013; 28: 407–418.

Appendix

Direction cosines and weights for different utilized integration schemes

The weights and direction cosines for O21, NO21, O33, O37, and NO61 integration formulations are presented in Tables 2 to 6.[52]

Table 2. Direction cosines and weights for O21 integration formula.[52]

k	ζ_1^k	ζ_2^k	ζ_3^k	w^k
1	1.000000000000	0.000000000000	0.000000000000	0.026521424409
2	0.000000000000	1.000000000000	0.000000000000	0.026521424409
3	0.000000000000	0.000000000000	1.000000000000	0.026521424409
4	0.707106781187	0.707106781187	0.000000000000	0.019930147631
5	0.707106781187	−0.707106781187	0.000000000000	0.019930147631
6	0.707106781187	0.000000000000	0.707106781187	0.019930147631
7	0.707106781187	0.000000000000	−0.707106781187	0.019930147631
8	0.000000000000	0.707106781187	0.707106781187	0.019930147631
9	0.000000000000	0.707106781187	−0.707106781187	0.019930147631
10	0.387907304067	0.387907304067	0.836095596749	0.025071236749
11	0.387907304067	0.387907304067	−0.836095596749	0.025071236749
12	0.387907304067	−0.387907304067	0.836095596749	0.025071236749
13	0.387907304067	−0.387907304067	−0.836095596749	0.025071236749
14	0.387907304067	0.836095596749	0.387907304067	0.025071236749
15	0.387907304067	0.836095596749	−0.387907304067	0.025071236749
16	0.387907304067	−0.836095596749	0.387907304067	0.025071236749
17	0.387907304067	−0.836095596749	−0.387907304067	0.025071236749
18	0.836095596749	0.387907304067	0.387907304067	0.025071236749
19	0.836095596749	0.387907304067	−0.387907304067	0.025071236749
20	0.836095596749	−0.387907304067	0.387907304067	0.025071236749
21	0.836095596749	−0.387907304067	−0.387907304067	0.025071236749

Table 3. Direction cosines and weights for NO21 integration formula.[52]

k	ζ_1^k	ζ_2^k	ζ_3^k	w^k
1	0.187592474085	0.000000000000	0.982246946377	0.019841269841
2	0.794654472292	−0.525731112119	0.303530999103	0.019841269841
3	0.794654472292	0.525731112119	0.303530999103	0.019841269841
4	0.187592474085	−0.850650808352	−0.491123473188	0.019841269841
5	0.794654472292	0.000000000000	−0.607061998207	0.019841269841
6	0.187592474085	0.850650808352	−0.491123473188	0.019841269841
7	0.577350269190	−0.309016994375	0.755761314076	0.025396825397
8	0.577350269190	0.309016994375	0.755761314076	0.025396825397
9	0.934172358963	0.000000000000	0.356822089773	0.025396825397
10	0.577350269190	−0.809016994375	−0.110264089708	0.025396825397
11	0.934172358963	−0.309016994375	−0.178411044887	0.025396825397
12	0.934172358963	0.309016994375	−0.178411044887	0.025396825397
13	0.577350269190	0.809016994375	−0.110264089708	0.025396825396
14	0.577350269190	−0.500000000000	−0.645497224368	0.025396825397
15	0.577350269190	0.500000000000	−0.645497224368	0.025396825397
16	0.356822089773	−0.809016994375	0.467086179481	0.025396825397
17	0.356822089773	0.000000000000	−0.934172358963	0.025396825397
18	0.356822089773	0.809016994375	0.467086179481	0.025396825397
19	0.000000000000	−0.500000000000	0.866025403784	0.025396825397
20	0.000000000000	−0.500000000000	−0.866025403784	0.025396825397
21	0.000000000000	1.000000000000	0.000000000000	0.025396825397

Table 4. Direction cosines and weights for O33 integration formula.[52]

k	ζ_1^k	ζ_2^k	ζ_3^k	w^k
1	1.000000000000	0.000000000000	0.000000000000	0.009853539934
2	0.000000000000	1.000000000000	0.000000000000	0.009853539934
3	0.000000000000	0.000000000000	1.000000000000	0.009853539934
4	0.707106781187	0.707106781187	0.000000000000	0.016296968589
5	0.707106781187	−0.707106781187	0.000000000000	0.016296968589
6	0.707106781187	0.000000000000	0.707106781187	0.016296968589
7	0.707106781187	0.000000000000	−0.707106781187	0.016296968589
8	0.000000000000	0.707106781187	0.707106781187	0.016296968589
9	0.000000000000	0.707106781187	−0.707106781187	0.016296968589
10	0.933898956394	0.357537045978	0.000000000000	0.013478884401
11	0.933898956394	−0.357537045978	0.000000000000	0.013478884401
12	0.357537045978	0.933898956394	0.000000000000	0.013478884401
13	0.357537045978	−0.933898956394	0.000000000000	0.013478884401
14	0.933898956394	0.000000000000	0.357537045978	0.013478884401
15	0.933898956394	0.000000000000	−0.357537045978	0.013478884401
16	0.357537045978	0.000000000000	0.933898956394	0.013478884401
17	0.357537045978	0.000000000000	−0.933898956394	0.013478884401
18	0.000000000000	0.933898956394	0.357537045978	0.013478884401
19	0.000000000000	0.933898956394	−0.357537045978	0.013478884401
20	0.000000000000	0.357537045978	0.933898956394	0.013478884401
21	0.000000000000	0.357537045978	−0.933898956394	0.013478884401
22	0.437263676092	0.437263676092	0.785875915868	0.017575912988
23	0.437263676092	0.437263676092	−0.785875915868	0.017575912988

(continued)

Table 4. Continued

k	ζ_1^k	ζ_2^k	ζ_3^k	w^k
24	0.437263676092	−0.437263676092	0.785875915868	0.017575912988
25	0.437263676092	−0.437263676092	−0.785875915868	0.017575912988
26	0.437273676092	0.785875915868	0.437263676092	0.017575912988
27	0.437263676092	0.785875915868	−0.437263676092	0.017575912988
28	0.437263676092	−0.785875915868	0.437263676092	0.017575912900
29	0.437263676092	−0.785875915868	−0.437263676092	0.017575912988
30	0.785875915868	0.437263676092	0.437263676092	0.017575912988
31	0.785875915868	0.437263676092	−0.437263676092	0.017575912988
32	0.785875915868	−0.437263676092	0.437263676092	0.017575912988
33	0.785875915868	−0.437263676092	−0.437263676092	0.017575912988

Table 5. Direction cosines and weights for O37 integration formula.[52]

k	ζ_1^k	ζ_2^k	ζ_3^k	w^k
1	1.000000000000	0.000000000000	0.000000000000	0.010723885730
2	0.000000000000	1.000000000000	0.000000000000	0.010723885730
3	0.000000000000	0.000000000000	1.000000000000	0.010723885730
4	0.707106781187	0.707106781187	0.000000000000	0.021141609520
5	0.707106781187	−0.707106781187	0.000000000000	0.021141609520
6	0.707106781187	0.000000000000	0.707106781187	0.021141609520
7	0.707106781187	0.000000000000	−0.707106781187	0.021141609520
8	0.000000000000	0.707106781187	0.707106781187	0.021000000000
9	0.000000000000	0.707106781187	−0.707106781187	0.021141609520
10	0.951077869651	0.308951267775	0.000000000000	0.005355055908
11	0.951077869651	−0.308951267775	0.000000000000	0.005355055908
12	0.308951267775	0.951077869651	0.000000000000	0.005355055908
13	0.308951267775	−0.951077869651	0.000000000000	0.005355055908
14	0.951077869651	0.000000000000	0.308951267775	0.005355055908
15	0.951077869651	0.000000000000	−0.308951267775	0.005355055908
16	0.308951267775	0.000000000000	0.951077869651	0.005355055908
17	0.308951267775	0.000000000000	−0.951077869651	0.005355055908
18	0.000000000000	0.951077869651	0.308951267775	0.005355055908
19	0.000000000000	0.951077869651	−0.308951267775	0.005355055908
20	0.000000000000	0.308951267775	0.951077869651	0.005355055908
21	0.000000000000	0.308951267775	−0.951077869651	0.005355055908
22	0.335154591939	0.335154591939	0.880535518310	0.016777090916
23	0.335154591939	0.335154591939	−0.880535518310	0.016777090916
24	0.355154591939	−0.335154591939	0.880535518310	0.016777090916
25	0.335154591939	−0.335154591939	−0.880535518310	0.016777090916
26	0.335154591939	0.880535518310	0.335154591939	0.016777090916
27	0.335154591939	0.880535518310	−0.335154591939	0.016777090916
28	0.335154591939	−0.880535518310	0.335154591939	0.016777090916
29	0.335154591939	−0.880535518310	−0.335154591939	0.016777090916
30	0.880535518310	0.335154591939	0.335154591939	0.016777090916
31	0.880535518310	0.335154591939	−0.335154591939	0.016777090916
32	0.880535518310	−0.335154591939	0.335154591939	0.016777090916
33	0.880535518310	−0.335154591939	−0.335154591939	0.016777090916
34	0.577350269190	0.577350269190	0.577350269190	0.018848230951
35	0.577350269190	0.577350269190	−0.577350269190	0.018848230951
36	0.577350269190	−0.577350269190	0.577350269190	0.018848230951
37	0.577350269190	−0.577350269190	−0.577350279190	0.018848230951

Table 6. Direction cosines and weights for NO61 integration formula.[52]

k	ζ_1^k	ζ_2^k	ζ_3^k	w^k
1	1.000000000000	0.000000000000	0.000000000000	0.007958442047
2	0.745355992500	0.000000000000	0.666666666667	0.007958442047
3	0.745355992500	−0.577350279190	−0.333333333333	0.007958442047
4	0.745355992500	0.577350269190	−0.333333333333	0.007958442047
5	0.333333333333	0.577350279190	0.745355992500	0.007958442047
6	0.333333333333	−0.577350269190	0.745355992500	0.007958442047
7	0.333333333333	−0.934172358963	0.127322003750	0.007958442047
8	0.333333333333	−0.356822089773	−0.872677996250	0.007958442047
9	0.333333333333	0.356822089773	−0.872677996250	0.007958442047
10	0.333333333333	0.934172358963	0.127322003750	0.007958442047
11	0.794654472292	−0.525731112119	0.303530999103	0.010515524289
12	0.794654472292	0.000000000000	−0.607061998207	0.010515524289
13	0.794654472292	0.525731112119	0.303530999103	0.010515524289
14	0.187592474085	0.000000000000	0.982246946377	0.010515524289
15	0.187592474085	−0.850650808352	−0.491123473188	0.010515524289
16	0.187592474085	0.850650808352	−0.491123473188	0.010515524389
17	0.934172358963	0.000000000000	0.356822089773	0.010011936427
18	0.934172358963	−0.309016994375	−0.178411044887	0.010011936427
19	0.934172358963	0.309016994375	−0.178411044887	0.010011936427
20	0.577350269190	0.309016994375	0.755761314076	0.010011936427
21	0.577350269190	−0.309016994375	0.755761314076	0.010011936427
22	0.577350269190	−0.809016994375	−0.110264089708	0.010011936427
23	0.577350269190	−0.500000000000	−0.645497224368	0.010011936427
24	0.577350269190	0.500000000000	−0.645497224368	0.010011936426
25	0.577350269190	0.809016994375	−0.110264089708	0.010011936427
26	0.356822089773	−0.809016994375	0.467086179481	0.010011936427
27	0.356822089773	0.000000000000	−0.934172358963	0.010011936427
28	0.356822089773	0.809016994375	0.467086179481	0.010011936427
29	0.000000000000	0.500000000000	0.866025403784	0.010011936427
30	0.000000000000	−1.000000000000	0.000000000000	0.010011936427
31	0.000000000000	0.500000000000	−0.866025403784	0.010011936427
32	0.947273580412	−0.277496978165	0.160212955043	0.006904779580
33	0.812864676392	−0.277496978165	0.512100034157	0.006904779580
34	0.595386501297	−0.582240127941	0.553634669695	0.006904779580
35	0.595386501297	−0.770581752342	0.227417407053	0.006904779580
36	0.812864676392	−0.582240127941	−0.015730584514	0.006904779580
37	0.492438766306	−0.753742692223	0.435173546254	0.006904779580
38	0.274960591212	−0.942084316623	−0.192025554687	0.006904779580
39	-0.076926487903	−0.942084316623	−0.326434458707	0.006904779580
40	-0.076926487903	−0.753742692223	−0.652651721349	0.006904779580
41	0.274960591212	−0.637341166847	−0.719856173359	0.006904779580
42	0.947273580412	0.000000000000	−0.320425910085	0.006904779580
43	0.812864676392	−0.304743149777	−0.496369440643	0.006904779580
44	0.595386501297	−0.188341624401	−0.781052076747	0.006904779580
45	0.595386501297	0.188341624401	−0.781052076747	0.006904779480
46	0.812864676392	0.304743149777	−0.496369449643	0.006904779580
47	0.492438766306	0.753742692223	−0.435173546254	0.006904779580
48	0.274960591212	0.637341166847	−0.719856173359	0.006904779580
49	-0.076926487903	0.753742692223	−0.652651721349	0.006904779580
50	-0.076926487903	0.942084316623	−0.326434458707	0.006904779580

(continued)

Table 6. Continued

k	ζ_1^k	ζ_2^k	ζ_3^k	w^k
51	0.274960591212	0.942084316623	−0.192025554687	0.006904779580
52	0.947273580412	0.277496978165	0.160212955043	0.006904779580
53	0.812864676392	0.582240127941	−0.015730584514	0.006904779580
54	0.595386501297	0.770581752342	0.227417407053	006904779580
55	0.595386501297	0.582240127941	0.553634669695	0.006904779580
56	0.812864676392	0.277496978165	0.512100034157	0.006904779580
57	0.492438766306	0.000000000000	0.870347092509	0.006904779580
58	0.274960591212	0.304743149777	0.911881728046	0.006904779580
59	-0.076926487903	0.188341624401	0.979086180056	0.006904779580
60	-0.076926487903	−0.188341624401	0.979086180056	0.006904779580
61	0.274960591212	−0.304743149777	0.911881728046	0.006904779580